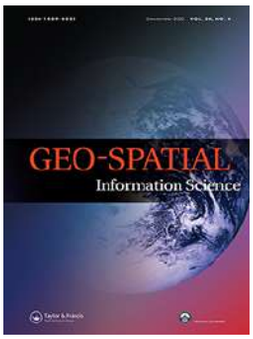

Geo-spatial Information Science

ISSN: (Print) (Online) Journal homepage: https://www.tandfonline.com/loi/tgsi20

Multi-sensor InSAR time series fusion for long-term land subsidence monitoring

Haonan Jiang, Timo Balz, Francesca Cigna, Deodato Tapete, Jianan Li & Yakun Han

To cite this article: Haonan Jiang, Timo Balz, Francesca Cigna, Deodato Tapete, Jianan Li & Yakun Han (2023): Multi-sensor InSAR time series fusion for long-term land subsidence monitoring, Geo-spatial Information Science, DOI: 10.1080/10095020.2023.2178337

To link to this article: https://doi.org/10.1080/10095020.2023.2178337

Published online: 17 May 2023.

GEO-SPATIAL INFORMATION SCIENCE
https://doi.org/10.1080/10095020.2023.2178337

Taylor & Francis
Taylor & Francis Group

Multi-sensor InSAR time series fusion for long-term land subsidence monitoring

Haonan Jiang [a,b], Timo Balz [a], Francesca Cigna [c], Deodato Tapete [d], Jianan Li [e] and Yakun Han [f]

[a]State Key Laboratory of Information Engineering in Surveying, Mapping and Remote Sensing (LIESMARS), Wuhan University, Wuhan, China; [b]Helmholtz Centre Potsdam, GFZ German Research Centre for Geosciences, Potsdam, Germany; [c]Institute of Atmospheric Sciences and Climate (ISAC), National Research Council (CNR), Roma, Italy; [d]Italian Space Agency (ASI), Roma, Italy; [e]Institute for Remote Sensing Science and Application, School of Geomatics, Liaoning Technical University, Fuxin, China; [f]College of Earth Science, Chengdu University of Technology, Chengdu, China

ABSTRACT

Satellite Interferometric Synthetic Aperture Radar (InSAR) is widely used for topographic, geological and natural resource investigations. However, most of the existing InSAR studies of ground deformation are based on relatively short periods and single sensors. This paper introduces a new multi-sensor InSAR time series data fusion method for time-overlapping and time-interval datasets, to address cases when partial overlaps and/or temporal gaps exist. A new Power Exponential Knothe Model (PEKM) fits and fuses overlaps in the deformation curves, while a Long Short-Term Memory (LSTM) neural network predicts and fuses any temporal gaps in the series. Taking the city of Wuhan (China) as experiment area, COSMO-SkyMed (2011–2015), TerraSAR-X (2015–2019) and Sentinel-1 (2019–2021) SAR datasets were fused to map long-term surface deformation over the last decade. An independent 2011–2020 InSAR time series analysis based on 230 COSMO-SkyMed scenes was also used as reference for comparison. The correlation coefficient between the results of the fusion algorithm and the reference data is 0.87 in the time overlapping region and 0.97 in the time-interval dataset. The correlation coefficient of the overall results is 0.78, which fully demonstrates that the algorithm proposed in our paper achieves a similar trend as the reference deformation curve. The experimental results are consistent with existing studies of surface deformation at Wuhan, demonstrating the accuracy of the proposed new fusion method to provide robust time series for the analysis of long-term land subsidence mechanisms.

ARTICLE HISTORY
Received 22 September 2022
Accepted 6 February 2023

KEYWORDS
Interferometric Synthetic Aperture Radar (InSAR); Power Exponential Knothe Model (PEKM); Long Short-Term Memory Network (LSTM); data fusion

1. Introduction

Consolidation and compression of soft soil layers under the joint action of natural and human factors (Bagheri-Gavkosh et al. 2021) can cause irreversible damage to urban infrastructure, including buildings (Abidin et al. 2011), roads (Chen et al. 2021), and underground pipelines (Perissin, Wang, and Lin 2012). This is a common engineering geological problem in major cities all over the world (Ding et al. 2021; Herrera-García et al. 2021), requiring detailed characterization and monitoring, as well as development of mitigation measures to reduce impacts on urban assets.

Traditional monitoring tools (e.g. leveling, Global Positioning System – GPS), and other field observation methods used for urban subsidence monitoring, are mostly point-based methods with typically low spatial (and partly temporal) density of observations, long sampling time interval and limited applicability for large-scale monitoring (Han et al. 2020; Zhou et al. 2022). With the continuous development of remote sensing technology, Interferometric Synthetic Aperture Radar (InSAR) techniques have the advantage of high spatial and temporal resolution and wide coverage of SAR imagery (Zebker and Goldstein 1986). Therefore, these techniques have been widely used in urban surface deformation monitoring since the 1990s and have now become well-established subsidence monitoring tools (Cigna and Tapete 2021; Haghshenas Haghighi and Motagh 2019; Zhou et al. 2022; Ma et al. 2022; Orhan 2021; Orhan et al. 2021; Sun et al. 2016; Zhu et al. 2015), providing outputs of suitable accuracy (Cigna, Ramírez, and Tapete 2021). In the process of application, the traditional Differential InSAR (DInSAR) has gradually developed into advanced multi-temporal methods, such as Persistent Scatterer InSAR (PS-InSAR) (Ferretti, Prati, and Rocca 2000, 2001) and Small Baseline Subset (SBAS) (Berardino et al. 2002; Lanari et al. 2004).

Due to the generally limited nominal lifespan of a single SAR satellite (e.g. 5–7 years) and observation scenarios by which long SAR time series over the same area on the ground are possible but not always available, most existing InSAR studies cover a limited time period only (mostly short-term studies of 1–5

CONTACT Timo Balz balz@whu.edu.cn

years). Taking the city of Wuhan, China, as an example of a fast-expanding city where land subsidence is strongly related to urban development and, as such, was repeatedly investigated by the InSAR community, Costantini et al. (2016) and Zhou et al. (2017) all used image datasets with a length of one year to monitor short-term subsidence and analyze the spatio-temporal features and causes of deformation. Han et al. (2020) used the PS-InSAR method to process Envisat 2008–2010, ALOS-1 2007–2010, and Sentinel-1 (S1) 2015–2019 images, and analyzed the effects of urban construction, changes in Yangtze River and ground water levels, on the subsidence patterns and trends across the city. Although multiple datasets were included, these data are not continuous and thus processed and analyzed in segments. Hu et al. (2021) used the SBAS method to analyze consolidation of soft soil and karst collapse hazards in Wuhan using TerraSAR-X (TSX) imagery collected in 2013–2017 and S1 imagery in 2015–2017. The segmental processing approach was employed, however, thus only revealing short-term change and not exploring long-term changes over time. The longest InSAR study of land subsidence in Wuhan based on a continuous time series is the analysis by Jiang et al. (2021) using COSMO-SkyMed (CSK) data from 2012 to 2019. However, for a slowly developing geologic hazard like surface subsidence, observations spanning over a decade would be recommended to accurately determine long-term trends and the induced risk level on urban infrastructure, especially in cities where multiple processes and different timings of urban development may occur. Therefore, time series fusion of InSAR datasets derived from multiple satellite platforms is of strategic importance (Chen et al. 2021).

Several studies have focused on multi-sensor data fusion. Samsonov and D'Oreye (2012) used singular value decomposition (SVD) combined with Tikhonov regularization to fuse multi-sensor SBAS subsidence results. Deng et al. (2016) used nonlinear deformation model constrained SBAS analysis to fuse multi-sensor data. Pepe et al. (2016) regularized the underdetermined system of linear equations to get the minimum acceleration of (unknown) 3-D deformation components to complete the fusion of multi-sensor data. Sun et al. (2016) merged different InSAR results by considering the offset over overlapping areas. Haghshenas Haghighi and Motagh (2019) fused InSAR datasets by assuming that different time series follow the same trend line. Yastika, Shimizu, and Abidin (2019) used a hyperbolic method for multi-sensor data fusion. Chen et al. (2021) fused SBAS results from two sensors using a time series approach based on the minimum gradient difference. These methods either exploit model-constrains or assume a linear trend of the subsidence curve. However, the long-term subsidence curves might be influenced by various factors and often show nonlinear characteristics (e.g. in Wuhan (Jiang et al. 2021), Aguascalientes (Cigna and Tapete 2021)). In addition, depending on the input data collected, there may be overlaps and/or gaps between the different datasets composing the time series. Both circumstances can impact data fusion.

In this paper, a nonlinear PS-InSAR method is used to process three SAR image datasets separately, and a multi-source and multi-case InSAR deformation data fusion method combining the Power Exponential Knothe Model (PEKM) (Chen et al. 2018) with the Long Short-Term Memory (LSTM) neural network (Chen et al. 2022, 2021; Ding et al. 2021; Qu, Yang, and Chang 2019) is proposed to fuse the datasets, to obtain the longest deformation time series results for the city. The method preserves the nonlinear characteristics in the long-term deformation curve. The tests were undertaken by simulating two cases, i.e. when InSAR time series from different sensors partially overlap in time, and when there is a temporal gap of data in between, to prove that the method is also suitable for "multi-case" implementation. The new method enables obtaining long deformation time series from multi-sensor datasets.

2. Methodology

PS-InSAR is used to process SAR single look complex images using SARPROZ software to obtain PS datasets with associated line-of-sight (LOS) displacement time series and velocities for the research area. These are the inputs that are used for the fusion experiments. Two main aspects need to be accounted for before fusion:

(1) The coordinate systems of the PS datasets resulting from the processing of multi-sensor SAR imagery are different, and so are the incidence angle, spatial resolution, and other parameters of the images. Simple calculation of the algebraic sum of deformation values measured by multiple sensors may cause errors. Therefore, the unification of the reference datum (e.g. all datasets are projected to the WGS84 geographic reference system) is required before multi-source SAR data can be fused.
(2) Land subsidence often evolves by following a nonlinear trend. As a consequence, the simplest linear time series fusion approach may give poor fusion performance. Therefore, a nonlinear model needs to be incorporated into the fusion workflow.

In the next sections, we explain how we first unify the coordinates of the different PS datasets, and post-process them to retrieve vertical time series deformation.

The two cases of data fusion methods (namely, when the time series show overlapping periods, and when they exhibit temporal gaps) are then discussed in depth.

2.1. PS-InSAR analysis and post-processing

The standard PS-InSAR (Ferretti, Prati, and Rocca 2000, 2001) technique and SARPROZ (Perissin, Wang, and Lin 2012; Roccheggiani et al. 2019) software are used to process the datasets. The quality parameters describing signal stability of radar targets are combined to get PS points. Height and velocity parameters are estimated by means of a strong first-order network comprising a sub-selection of PS candidates (PSC) (with amplitude stability index, ASI $>$ 0.8), where atmospheric phase components are detected and removed. The LOS deformation rate and time series are estimated for each point using a nonlinear trend model. The output dataset resulting from the high resolution sensors (onboard TSX and CSK) are resampled to the result of the low-resolution sensor (S1) to a same final resolution of 30 m.

PS deformation values in the LOS direction is shown in Equation (1):

$$D_{LOS} = \cos\theta \cdot D_U + \sin\theta \cdot \sin\varphi \cdot D_N - \sin\theta\cos\varphi \cdot D_E \quad (1)$$

where $D_U = [D_{U_1}, D_{U_2}, \ldots, D_{U_n}]$, $D_N = [D_{N_1}, D_{N_2}, \ldots, D_{N_n}]$, $D_E = [D_{E_1}, D_{E_2}, \ldots, D_{E_n}]$ are the three-dimensional cumulative deformation components along the vertical, north-south and east-west direction, respectively. The value θ represents the incidence angle of the sensor, and φ represents the corresponding orbit azimuth angle. The SAR image orbit is near-polar, therefore the sensitivity of the estimations to the north-south motion is quite limited. Meanwhile, assuming that the east-west deformation component can be neglected, the vertical deformation component can be obtained from the LOS measurement as:

$$D_U \cong \frac{D_{LOS}}{\cos\theta} \quad (2)$$

2.2. Data fusion approach

2.2.1. Case 1: time series overlaps

Non-linear deformation behavior dominates in long time series of urban surface subsidence because of various influences, such as human activities and natural factors; therefore, the general linear model may not always meet the specific needs of a subsidence study. The a priori model can be derived from the urban deformation characteristics. During the initial stage of surface settlement, cumulative deformation grows relatively rapidly, and the settlement velocity increases with time. This means that the surface settlement acceleration is positive at this stage. During the following stage, the settlement velocity gradually reaches the maximum. But the settlement acceleration gradually decreases to 0. During the decay stage of surface settlement, cumulative deformation continues to increase, but increases slowly. Thus, the settlement velocity gradually tends to 0 at this stage. Hence, the acceleration of subsidence gradually changes from a negative value to 0 (Stramondo et al. 2008; Pratesi et al. 2016; Lei et al. 2018; Xinru and Yuchan 2012).

From this analysis, it can be concluded that the whole stage morphology follows a roughly S-shaped curve. Therefore, we combine the nonlinear features of the surface settlement process, using the Power Exponential Knothe Mode (PEKM) model, which can better fit this deformation feature to completely capture the entire process (Lei et al. 2018; Xinru and Yuchan 2012). The surface subsidence in PEKM is shown in Equation (3):

$$W(t) = W_{\max}(1 - e^{-ct})^k \quad (3)$$

where $W(t)$ represents the cumulative deformation at time t, $W_{\max}$ is the predicted maximum deformation, and c, k are the shape parameters to be estimated. By deriving the model, the deformation velocity $v(t)$ and acceleration $a(t)$ can be expressed as (Liu, Cao, and Liu 2009):

$$v(t) = W_{\max}kce^{-ct}(1 - e^{-ct})^{k-1} \quad (4)$$

$$a(t) = -W_{\max}kc^2e^{-ct}(1 - e^{-ct})^{k-1} + W_{\max}k(k-1)c^2e^{-2ct}(1 - e^{-ct})^{k-2} \quad (5)$$

In order to show more intuitively that the model expresses the surface deformation process, the cumulative deformation, its velocity and acceleration curves over time as depicted by the PEKM model are displayed in Figure 1. This figure indicates that the model fits the subsidence curves for each stage of subsidence using different parameter settings.

The nonlinear least squares method combined with a genetic algorithm (GA) is used to estimate the three parameters (W_{max}, c, k) of the PEKM. The nonlinear least squares fitting algorithm is a local polar algorithm, which can quickly obtain a local polar solution, but not a global polar solution (Xing et al. 2022). A GA is a model for constructing artificial systems by imitating the mechanism of biological evolution. The method is self-organizing, self-adaptive, self-learning and essentially parallel, and has advantages when solving multi-dimensional, multi-peaked, and global optimization problems (Yao and Sethares 1994).

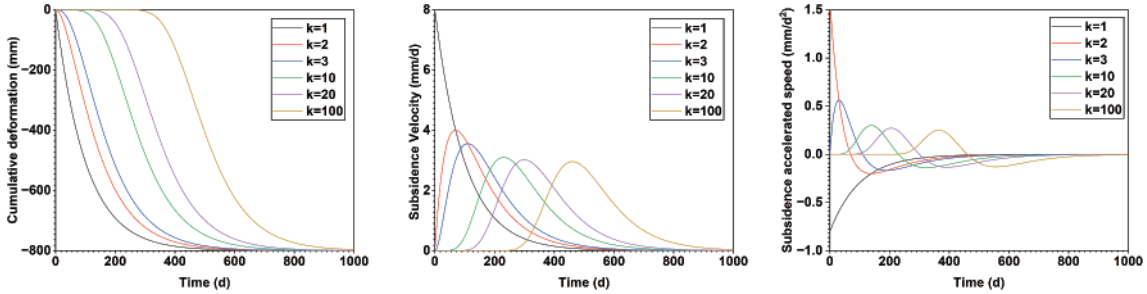

Figure 1. The influence of the shape parameter k in PEKM on (a) deformation value, (b) velocity and (c) acceleration.

A GA algorithm does not require much local information in order to determine the global optimal search direction, starting from the initial population, and evolving generation by generation to identify the optimal solution according to the natural biological evolution principle of survival of the fittest and superiority. In each generation, individuals are selected according to the magnitude of their fitness in the problem domain, and operations such as replication, exchange, and mutation are used to keep executing on and gradually approximating the global optimal solution (Xing et al. 2022).

Combining the PEKM and the GA simultaneously improves the global and convergence accuracy of the algorithm to obtain the global optimal solution. The fitness function is constructed from the 2-norm of the model residuals W_{res} at time t, which can be expressed as (Chen et al. 2021):

$$\text{Fitness} = \|\Delta W_{\text{res}}(t)\|_2^2 = \min \tag{6}$$

The main steps of the proposed method can be described as follows.

(1) Initialization. We determine the population size, hybridization probability, mutation rate, and termination iteration criterion, and then the number of individuals in the initial population randomly from them.
(2) Population evolution. Using the fitness function, we calculate the fitness of each individual in the population and assign a reproductive probability to each individual based on this fitness, and then perform genetic operations based on the set hybridization probability and mutation probability to form a new generation of population.
(3) Termination judgment. If the pre-set iteration termination criterion is satisfied, the computation is stopped and the optimal population of individuals is outputted and used as the final optimal parameter and the algorithm ends. If not, we return to step 2.
(4) The output approximate global optimal solution is brought into nonlinear least squares to obtain the global optimal solution.

2.2.2. Accurate determination of fusion time

After building fitting curves for the two time series datasets to fuse, we consider a more precise method to determine the fusion time t for the two curves. In many data fusion methods, this key issue is usually ignored, and the fusion time is randomly chosen or simply by the start/end time of the two datasets, which may affect the accuracy of fusion to a certain extent (Chen et al. 2021). Therefore, we determine the fusion time t by calculating the gradient of the two curves in the overlapping region, i.e. the minimum value of the velocity. The deformation curve trends are nearly the same when the gradient difference between the two curves is minimal, therefore that time was chosen as the fusion point. Thus, the fusion time t can be expressed as:

$$t = \arg\ \min\left\{\left|d_1'(t_i) - d_2'(t_i)\right|\right\}, t_i \in t_1 \cup t_2 \tag{7}$$

where d_1 and d_2 are the fitting curves of the subsidence time series of the two input datasets.

2.2.3. Case 2: temporal gaps

Unlike overlapping series, when there are temporal gaps between the two time-series to fuse, we consider an alternative fusion strategy. We employ an LSTM network to predict the subsidence trend during the gap and fuse it with the subsequent subsidence curves. LSTM is a particular kind of Recurrent Neural Network (RNN) (Sherstinsky 2020), which can effectively avoid the problem of gradient disappearance and explosion, which can occur when using RNNs due to their inability to transmit long-term information, as there is no gating mechanism (Gers, Schmidhuber, and Cummins 1999; Hochreiter and Schmidhuber 1997). Furthermore, LSTM efficiently stores information and provides more precise access to historical information. The network structure of LSTM is largely the same as that of RNN. However, unlike RNN, LSTM contains an external self-looping module, as well as an implicit layer that adds a "cell state". This layer contains several storage cells and three different gates module: input, forget, and output gates. These control historical information, collect external data, filter internal data, and control the retention of information (Qu, Yang, and Chang

2019). The gate module is controlled by a nonlinear activation function with a value between (0,1), indicating the proportion of information allowed to pass, which can be controlled to accumulate useful information over a longer period while selectively forgetting useless historical information. The interior of the cell state of the LSTM is shown in Figure 2.

As shown, the LSTM determines whether to forget or remember information from the previous cell state. The decision is made by the sigmoid layer "forget gate layer". The gate will read hidden state h_{t-1} at moment t-1 and the input x_t, and will output a value between 0 and 1, with 1 indicating completely retained and 0 indicating fully forgotten information (Qu, Yang, and Chang 2019).

$$f_t = \sigma\left(W_f \cdot [h_{t-1}, x_t] + b_f\right) \tag{8}$$

where σ represents the sigmoid activation function, W_f and b_f are the weights and deviations of the forgetting gate, respectively. After completing its judgment of the previous cell state, the LSTM determines what new information will be stored in the current cell state, which will be done by the input gate (Sherstinsky 2020).

The input gate controls the information x_t that is transmitted from the input of the network at moment t and hidden state at the final moment h_{t-1} to the cell state $\tilde{C}_t$. The "input gate layer" sigmoid layer identifies the values to update. Then, a hyperbolic tangent activation function (tanh) layer generates a vector of new candidate values to add to the state, which can be expressed as (Gers, Schmidhuber, and Cummins 1999):

$$i_t = \sigma(W_i \cdot [h_{t-1}, x_t] + b_i) \tag{9}$$

$$\tilde{C}_t = \tanh(W_C \cdot [h_{t-1}, x_t] + b_C) \tag{10}$$

where W_i and b_i correspond to the weights and the deviations of the sigmoid activation function in the input gate. W_C, refers to weights, while b_C represents the deviations of tanh in the input gate. The output of the two parts are multiplied together to get the updated cell state. To update the cell state, the old state is multiplied by f_t, thus forgetting what was forgotten earlier, and then it is added to the updated state to obtain $i_t * C_t$, and the cell state updating result C_t is obtained. The updating process can be expressed as (Gers, Schmidhuber, and Cummins 1999):

$$C_t = f_t \cdot C_{t-1} + i_t \cdot \tilde{C}_t \tag{11}$$

The LSTM neural network will decide what to output by running output gates to control the retention or non-retention of information in the current cell state. A sigmoid layer that decides what parts of the cell state to output is run. The cell state pushes the values between +1 and −1 through the tanh activation function, and multiplies i_t by the output of the sigmoid gate, consequently only outputting predetermined parts of the information. The calculation can be expressed as (Sherstinsky 2020):

$$O_t = \sigma(W_O \cdot [h_{t-1}, x_t] + b_O) \tag{12}$$

$$h_t = O_t \cdot \tanh(C_t) \tag{13}$$

The values W_O and b_O are the weight and deviation of the output gate, respectively.

The specific workflow of time series prediction combining PS-InSAR monitoring results and LSTM include:

(1) Data processing. Time series deformation data is first derived from PS-InSAR. It is transformed into an equal time interval data set using interpolation. Normalization of this dataset is carried out.
(2) Training the network. The first 90% of the dataset is used as the training set and the last 10% is kept as the test set. The Adam optimization function is used as the optimizer to update the network weights and initialize the model parameters. The mean square error is chosen as the model loss function, means of which are used to determine the reasonableness of the parameters.
(3) Prediction output. The trained network is used to predict the surface deformation and output the prediction results.

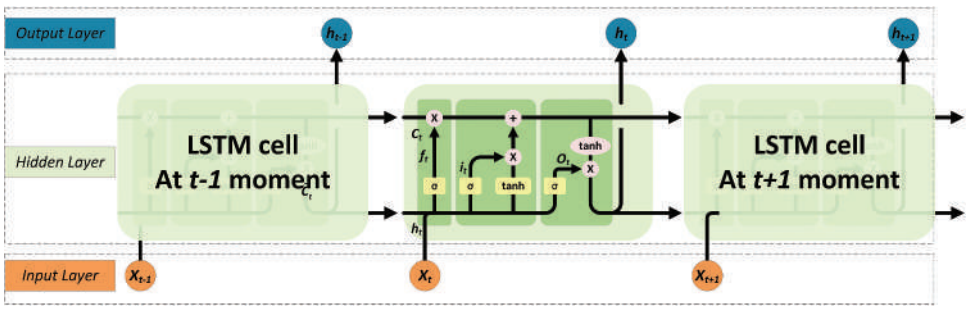

Figure 2. The basic computing unit structure of the LSTM model (Chen et al. 2021).

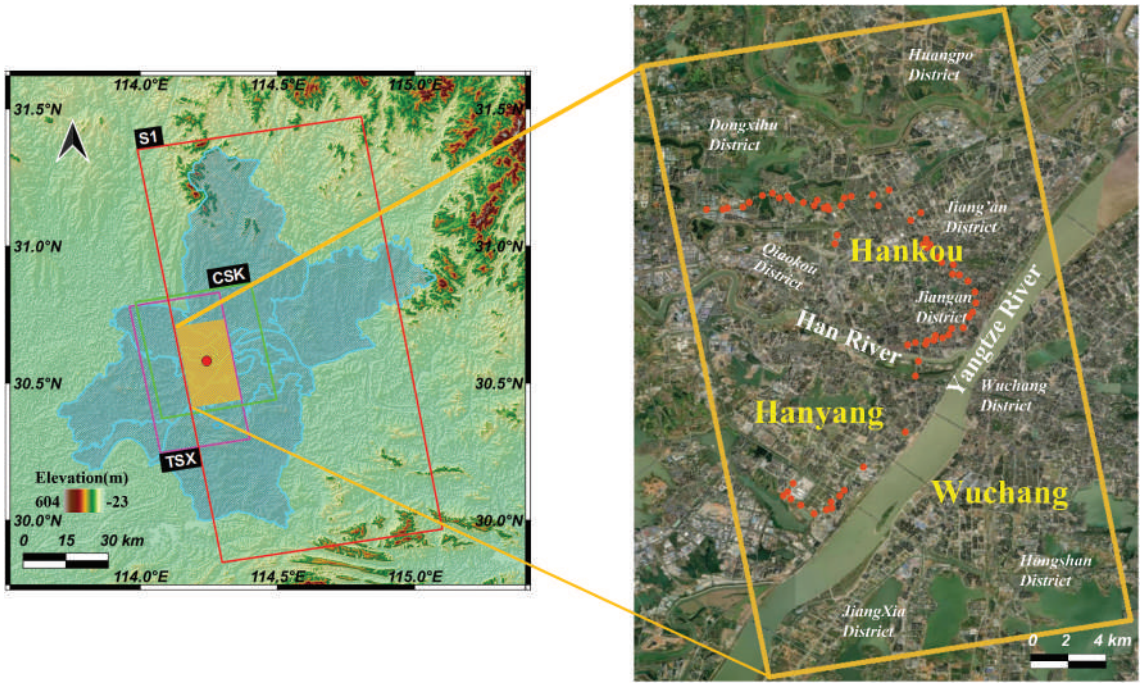

Figure 3. Research area of Wuhan, with outlined coverage of the three SAR data stacks used in this work (green polygon: COSMO-SkyMed – CSK; pink polygon: TerraSAR-X – TSX; and red polygon: Sentinel-1 – S1) and the regional boundaries of Wuhan (cyan polygons). The yellow rectangle with a red dot represents the selected study area. Key landmarks and place names are indicated onto Google Earth satellite imagery. The orange points are the 60 leveling benchmarks selected for accuracy verification.

3. Study area and datasets

The city of Wuhan (Figure 3), where land subsidence induced by urban development is a well-known process affecting the urban landscape and infrastructure (Jiang et al. 2021; Hu et al. 2022), was selected as experiment area. Using different datasets to simulate overlapping and gap regions in time series, these were then fused using the proposed algorithm, and combined to obtain the longest time-series deformation curves for Wuhan. Comparisons with existing studies are carried out to assess the quality of the results.

3.1. Study area

Wuhan is the largest city located in central China, with a resident population of about 13.6 million. The city is at the eastern edge of the Jianghan Plain, where the Yangtze River and its largest tributary, the Han River, divide it into three major urban areas, namely Hankou, Wuchang, and Hanyang (Tan et al. 2014; Wang, Balz, and Liao 2016).

Hankou is a major subsidence center in Wuhan, which has a history of subsidence for more than 10 years (Luo and Shen 2018; Zhou et al. 2017). Within this region, the Houhu area is the area most affected by ground deformation. This area has typical binary structure, with soft clay on top and sand below covering a thickness of 30–60 meters (Jiang et al. 2021; Hu et al. 2022). Subsidence in Hanyang and Hongshan has started to become apparent in recent years. In addition, soluble carbonates are widely distributed in most parts of these three districts and, together with human activities and other factors, the Wuhan area has been in a state of uneven settlement for a long time (Hu et al. 2021; Wang et al. 2020a). Figure 4 shows some examples of the structural impact caused by the subsidence process, gathered during our field investigations in Wuhan. If left unchecked, the continuous development of uneven settlement may pose a serious threat to urban properties of the city's inhabitants.

3.2. Input data

To explore the long-term subsidence trend in Wuhan, we collected three SAR data stacks composed of: 230 CSK images from the Italian Space Agency (ASI), 51 TSX images from the German Aerospace Center (DLR), and 30 S1 images from the European Space Agency (ESA), with coverage as shown in Figure 3 and detailed parameters listed in Table 1. It is worth noting that many more images (e.g. S1) were available in the archives and to the authors, but were intentionally not included in our experiment design.

The rationale was therefore to simulate different scenarios of data availability, overlaps and gaps. To this aim, we manually split the CSK dataset to stop at the end of 2015 and include only the first 89 scenes. As shown in Figure 5, there is a data overlap in the time series between the CSK and TSX datasets (i.e. January to December 2015), and a temporal gap

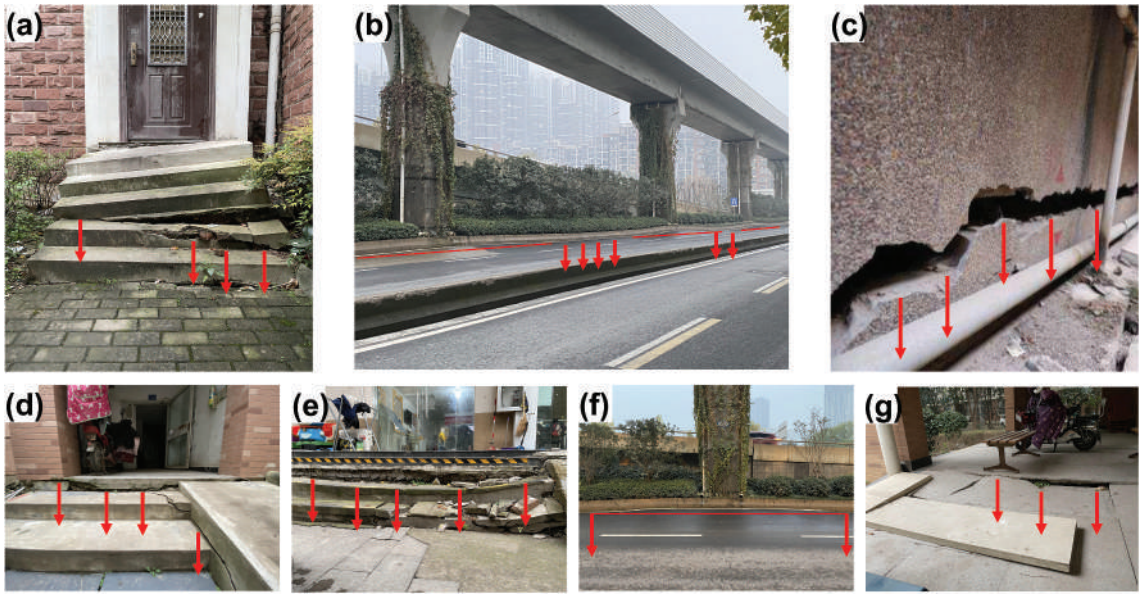

Figure 4. Field investigation showing noticeable cracks and discontinuities in the roads and building walls caused by the settlement. Photographs taken in September 2020; (b), (e) and (f) are from (Jiang et al. 2021).

Table 1. Key parameters of the three SAR datasets used for the data fusion analysis.

Satellite	COSMO-SkyMed	TerraSAR-X	Sentinel-1
Orbit direction	Ascending	Ascending	Ascending
Looking angle	23°	33.9°	36.9°
Ground resolution	3m	3m	30m
Band (wavelength)	X-Band (3.1 cm)	X-Band (3.1 cm)	C-Band (5.5 cm)
Number of images	89	51	30
Temporal coverage	29/05/2011–12/26/2015	14/01/2015–14/12/2018	13/06/2019–27/04/2021

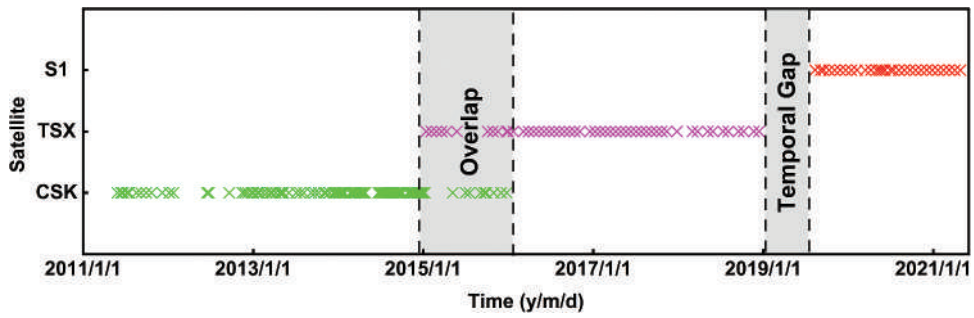

Figure 5. The three satellite datasets selected for the experiment.

between the TSX and S1 datasets (i.e. February to June 2019).

Additionally, a longer 2011–2020 CSK dataset of 230 scenes was also processed with the nonlinear PS-InSAR method, and used as a reference for comparison.

The 30 m resolution SRTM Digital Elevation Model (DEM) was used in the PS-InSAR processing to subtract the topographic phases. A total of 60 leveling benchmarks observations measured by the Wuhan Geomatics Institute in 2013–2014, 2015–2016, and 2019–2020 with about 2 mm of precision were selected to validate the InSAR-derived results. Optical images from Google Earth were exploited to match the period of the deformation time series.

4. Results and discussion

4.1. InSAR accuracy assessment

4.1.1. External compliance accuracy

To ensure comparability of the three processed datasets, we selected a similarly located PS point at the International GNSS Service (IGS) station to act as the reference point. To verify the accuracy of the PS-InSAR results, the estimated subsidence rates from the CSK, TSX and S1 datasets were compared with 60 leveling benchmark measurements (i.e. BM1-BM60) at corresponding times. Since the level points did not correspond exactly with the PS point positions, Kriging interpolation was first used to derive the subsidence record corresponding to each leveling point. A

linear regression was applied to the subsidence rates from the PS-InSAR analysis and the corresponding leveling measurements (Figure 6(a–c)), and the RMSE was calculated for the difference between the leveling and PS points (Figure 6(d–f)) by each of the three time periods.

The experiment proved that the three resulting datasets have a high correlation with leveling data with correlation coefficients (R) exceeding 80%, as shown in Figure 6(a–c). The differences between the InSAR and leveling data are mostly concentrated between −5 mm and +5 mm, as shown in Figure 6(d–f). Some

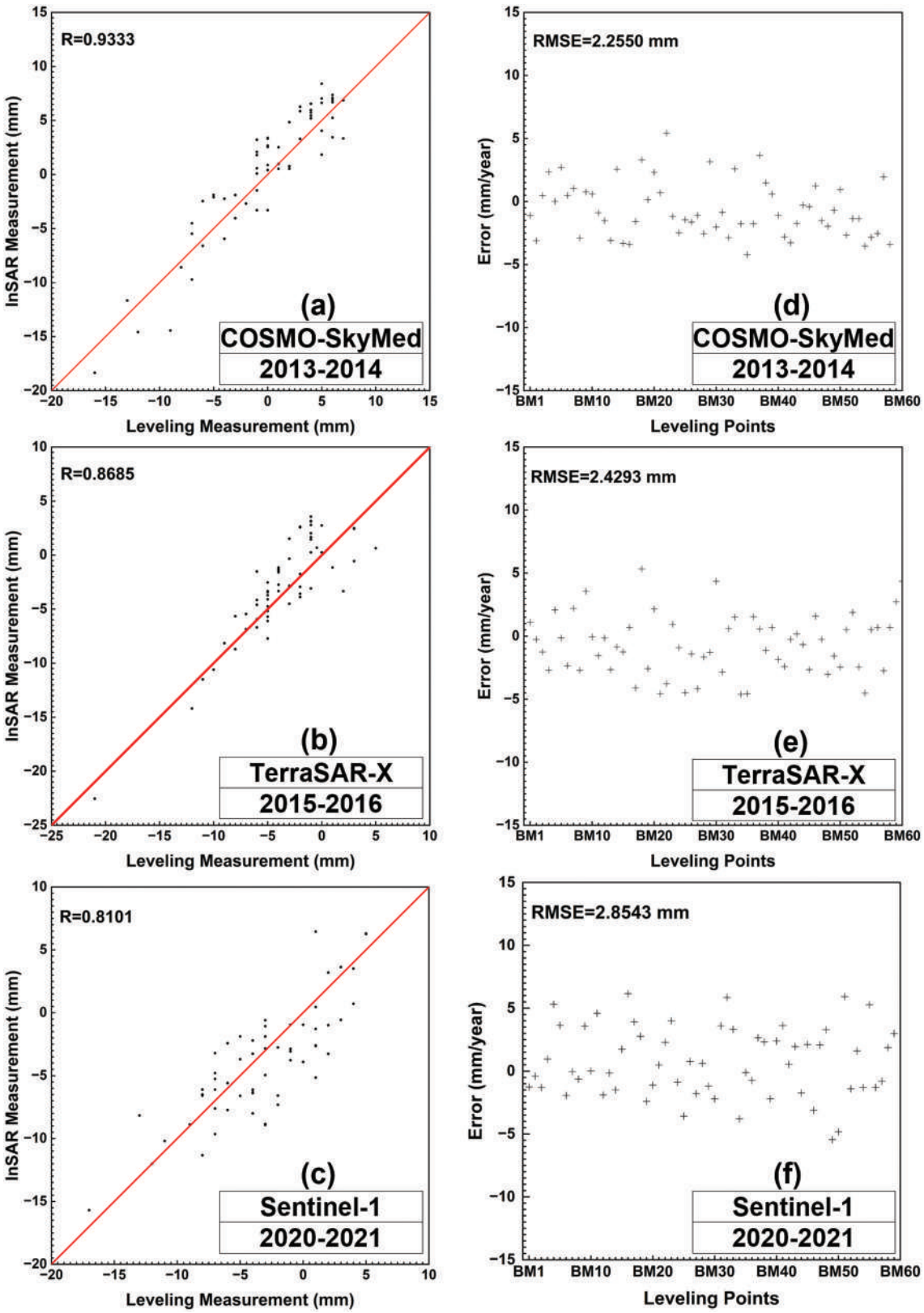

Figure 6. Comparison of leveling records and InSAR results. (a–c) Regression analysis between leveling observations and InSAR results. (d–f) Difference between leveling observations and InSAR results.

individual errors are larger. This is mainly caused by three factors. The InSAR results corresponding to the level point obtained by interpolation method are not completely consistent with the true value of the point, and the InSAR monitoring results are annual average rates over a period, which might be affected by seasonal variations. Moreover, the observation interval of the leveling data is one year, therefore the annual subsidence rates derived from leveling are only based on the difference between two epochs. Anyway, the observed maximum Root Mean Square Error (RMSE) of the three tests is only 2.85 mm, which demonstrates the high overall agreement between the InSAR results and the leveling data.

4.1.2. Internal compliance accuracy

The surface deformation of the three datasets was obtained by independent processing. Therefore, besides the accuracy assessment of each group of InSAR results and leveling points, the consistency of the subsidence results among the three datasets is also an important task in the accuracy assessment in order to prevent the influence on the accuracy of the fusion because of the observation error of processing each dataset separately. We extracted 60 targets of correspondence points, selected CSK observations throughout the fusion time range as the benchmark, and carried out error and standard deviation calculations with the observations of TSX and S1, and the accuracy evaluation results obtained are shown in Tables 2 and 3.

The TSX results for 2017–2019 were used to test against the CSK results. The precision evaluation is shown in Table 2. The maximum error is 4.99 mm, the minimum error is −4.88 mm, and the standard deviation is 2.9132 mm. The comparison results of S1 were slightly worse than TSX, which was related to its lower resolution. As shown in Table 3, with a maximum error of 9.81 mm, a minimum error of −3.69 mm, and a standard deviation of 3.3592 mm. This shows a strong overall agreement between the three independently processed datasets.

4.2. Results and discussion

4.2.1. Overlapping period

The deformation curve and fitting curve of a selected PS point in the CSK and TSX datasets are shown in Figure 7(a–b). The three parameters (W_{max}, c, k) of the PEKM estimated by nonlinear least squares method combined with GA are indicated in the figure. The Coefficient of Determination (R^2) for the two datasets is 0.9851 and 0.9812, which demonstrates the accuracy of the fit of the PEKM. As shown in Figure 7(c), the time t (02/12/2015) was identified as the minimum value of the gradient difference between the fitting

Table 2. Accuracy assessment of TSX and CSK deformation results from 2017–2019.

Point	CSK Cumulated deformation (mm)	TSX Cumulated deformation (mm)	Error (mm)	Point	CSK Cumulated deformation (mm)	TSX Cumulated deformation (mm)	Error (mm)
1	−27.35	−25.46	−1.89	31	−24.56	−22.51	−2.05
2 2	−21.97	−17.46	−4.51	32	−9.13	−8.93	−0.2
3 3	5.65	4.63	1.02	33	−6.63	−8.65	2.02
44	6.17	4.37	1.8	34	5.56	2.11	3.45
5 5	−5.38	−2.63	−2.75	35	−4.03	−5.6	1.57
6 6	−1.56	−3.7	2.14	36	9.47	7.62	1.85
77	−3.85	−5.58	1.73	37	−23.24	−18.42	−4.82
8 8	3.77	5.59	−1.82	38	3.02	0.48	2.54
99	0.99	0.89	0.1	39	−5.91	−7.24	1.33
110	−12.26	−10.58	−1.68	40	−15.08	−13.42	−1.66
111	−17.99	−13.97	−4.02	41	3.78	0.65	3.13
112	7.08	3.95	3.13	42	−21.1	−18.76	−2.34
113	−0.56	0	−0.56	43	6.85	3.17	3.68
114	−32.69	−28.52	−4.17	44	−18.59	−13.71	−4.88
115	−20.75	−18.24	−2.51	45	−2.75	0.58	−3.33
116	−2.56	−0.84	−1.72	46	−23.21	−19.48	−3.73
117	3.01	3.26	−0.25	47	−18.53	−20.71	2.18
118	2.8	7.59	−4.79	48	−12.73	−14.67	1.94
119	−32.04	−36.79	4.75	49	2.02	−1.75	3.77
220	−6.37	−9.45	3.08	50	−0.85	0	−0.85
221	−24.07	−27.51	3.44	51	−0.42	−0.45	0.03
222	7.11	5.89	1.22	52	7.79	6.15	1.64
223	−7.8	−5.32	−2.48	53	−3.12	−8.11	4.99
224	−15.07	−12.72	−2.35	54	−4.55	−4.85	0.3
225	−7.85	−10.26	2.41	55	−3.52	−1.16	−2.36
226	−2.08	−6.02	3.94	56	−7.94	−11.88	3.94
227	−19.22	−17.2	−2.02	57	−10.64	−8.1	−2.54
228	4.45	4.11	0.34	58	−19.98	−15.23	−4.75
229	−14.55	−11.66	−2.89	59	−7.72	−2.97	−4.75
330	−32.22	−33.16	0.94	60	−10.16	−14.88	4.72
Standard Deviation (mm)						2.9132	

Table 3. Accuracy assessment of S1 and CSK deformation results from 2019 to 2021.

Point	CSK Cumulated deformation (mm)	S1 Cumulated deformation (mm)	Error (mm)	Point	CSK Cumulated deformation (mm)	S1 Cumulated deformation (mm)	Error (mm)
1	−6.67	−0.31	6.36	31	−6.97	2.17	9.14
2 2	−10.27	−0.46	9.81	32	−5.26	−2.06	3.2
3 3	−3.84	−3.84	0	33	−2.71	−2.87	−0.16
4 4	−3.14	−1.78	1.36	34	−0.09	−2.19	−2.1
5 5	−8.43	−4.64	3.79	35	−3.45	−3.62	−0.17
6 6	−2.64	−0.45	2.19	36	−3.05	−3.42	−0.37
7 7	−3.39	−0.8	2.59	37	−11.06	−5.07	5.99
8 8	−6.63	−2.89	3.74	38	−2.23	−2.47	−0.24
9 9	−4.45	−1.49	2.96	39	−3.77	−0.56	3.21
110	−6.14	−2.39	3.75	40	−5.95	−2.29	3.66
111	−9.62	−1.1	8.52	41	−1.37	−0.18	1.19
112	−1.62	−3.28	−1.66	42	−7.13	−0.85	6.28
113	−5.7	−1.19	4.51	43	0.87	−1.14	−2.01
114	−10.22	−1.28	8.94	44	−12.59	−5.36	7.23
115	−7.81	−2.32	5.49	45	−9.06	−1.17	7.89
116	−6.49	−2.09	4.4	46	−9.57	−7	2.57
117	−5.31	−0.28	5.03	47	−2.37	−0.42	1.95
118	−11	−2.16	8.84	48	−2.92	−2.24	0.68
119	3.69	0	−3.69	49	1.33	1.65	0.32
220	−1.73	−0.74	0.99	50	−5.79	−5.52	0.27
221	−1.26	−1.93	−0.67	51	−4.87	−4.07	0.8
222	−3.78	−0.51	3.27	52	−3.43	−1.27	2.16
223	−7.26	−3.28	3.98	53	4.65	5.36	0.71
224	−7.14	−7.1	0.04	54	−4.42	−0.39	4.03
225	−2.27	−0.1	2.17	55	−7.26	−3.89	3.37
226	2.06	0.37	−1.69	56	2.55	0.07	−2.48
227	−6.82	−1.22	5.6	57	−8.11	0.02	8.13
228	−3.95	−2.71	1.24	58	−10.32	−2.69	7.63
229	−8.49	−5.9	2.59	59	−10.88	−2.6	8.28
330	−3.95	−2.85	1.1	60	3.49	2.66	−0.83
Standard Deviation (mm)						3.3592	

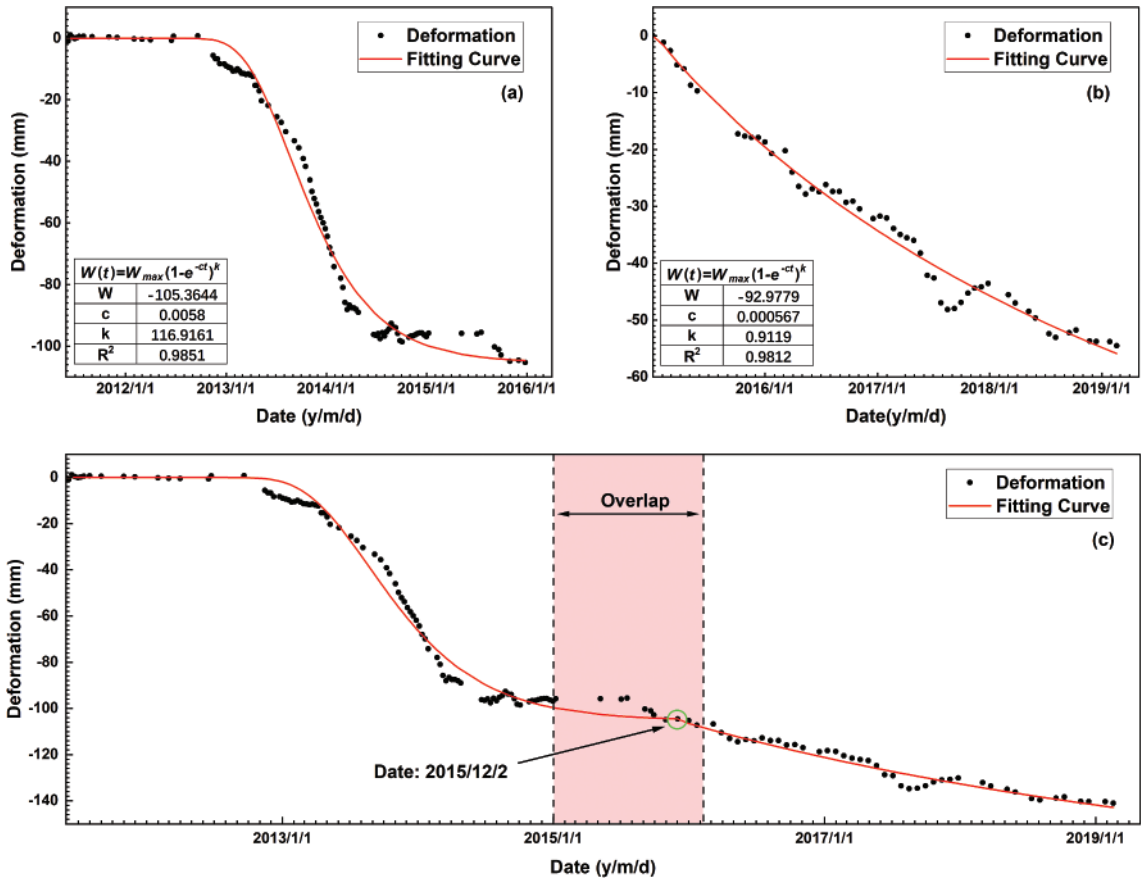

Figure 7. Overlapping period fitting and fusion results. (a) Fitting curve of COSMO-SkyMed, (b) fitting curve of TerraSAR-X, and (c) fusion result.

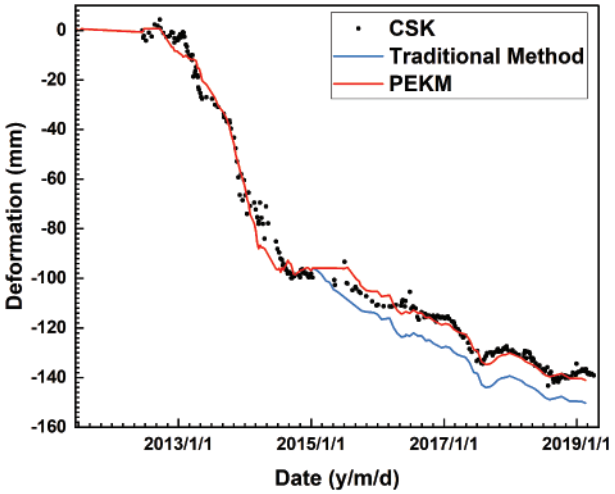

Figure 8. Comparison of the time series fusion results using the PEKM and conventional method with the full 2011–2019 time series obtained by processing the whole CSK dataset.

curves for the two input datasets. The deformation curves were fused at that point in time to obtain the fused series from 2011 to 2019.

To further verify the accuracy of the proposed algorithm, reference points were selected for comparative experiments. The fusion curves of PEKM and the conventional fusion algorithm were compared to the long-term deformation time series obtained by processing the whole 2011–2020 CSK dataset. The fused time series matches well with the reference 2011–2019 deformation curve (Figure 8). In contrast, traditional algorithms do not precisely consider the fusion point, and usually simply pick up the end time of the previous dataset or the start time of the second dataset as the fusion point. The traditional fusion method also follows the same trend of the reference curve, but does not take precise account of the fusion points. In this paper, the start time *t* (14/01/2015) of TSX, the second dataset, was chosen as the fusion point. It can be seen that the fusion point has a clear deformation offset which resulted in a cumulative error of more than 10 mm between the final fused and the reference curve. If multiple fusions are carried out, the errors will likely accumulate and gradually deviate from the reference value. Thus, there might be significant discrepancies starting in the year when the data are fused (i.e. 2015), developing with time and accumulating on the final generated settlement map, thus potentially causing a bias in the overall settlement magnitude and trend. Therefore, it is necessary to accurately consider the fusion point in the overlapping period to reduce the fusion error.

4.2.2. Temporal gaps

Based on the deformation curves obtained for the overlapping periods, the LSTM neural network prediction model predicts across temporal gaps, where data are missing. The cumulative vertical subsidence over t consecutive time periods (13 in this paper: $X_1, X_2, \ldots X_t$ in the first input block in Figure 9) is used as input in order to ensure that the deep learning model could learn reliable contextual features. For any moment after t such as t+1, the inputs to the model are the t continuous cumulative deformation values used to predict the deformation at t+1, and the output is the predicted deformation value X_t+1. In a recurrent neural network, the predicted value is then added to the input dataset to form a new input dataset with predictions of the subsidence at the next moment t+2. The specific prediction process is shown in Figure 9.

In each LSTM layer, the number of neurons was set to 50. The mean squared error (MSE) was used as the loss function. The gradient of MSE loss increases as the loss increases, and decreases when the loss tends to 0. Therefore, it has the property of fast convergence and accurate training results. We chose the computationally efficient Adam as the optimizer and the epoch was set to 70. The Adam algorithm records the First Moment Estimation of the gradient, i.e. the average of all past gradients and the current gradient, so that at each update, the gradient of the previous update is not

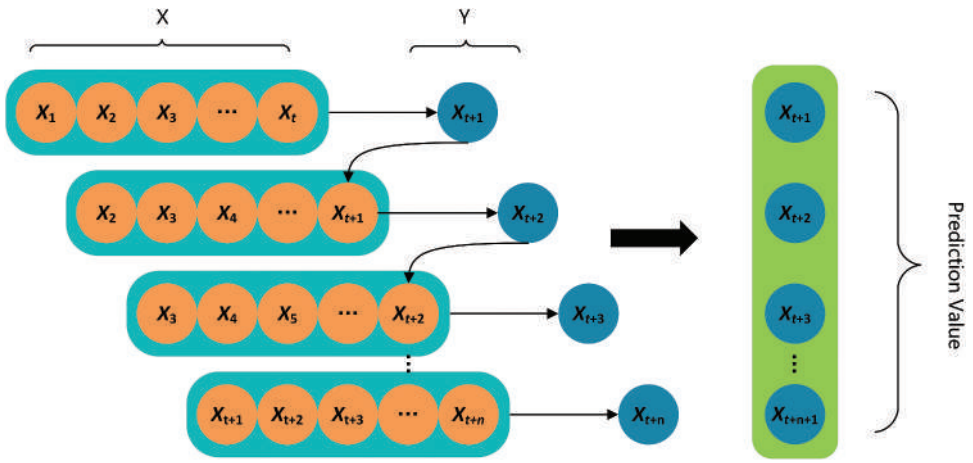

Figure 9. Network structure of the LSTM model to predict surface subsidence across temporal gaps in time series.

Table 4. Accuracy evaluation of LSTM model.

Evaluation Index	LSTM Model/(s)
RMSE (mm)	1.2296
MSE (mm)	1.1601
R^2	0.9437
MAE (mm)	1.4527

too different from the current update, i.e. the gradient has a smooth and stable transition that can accommodate unstable objective functions. Meanwhile, in order to verify the model accuracy, 70% of the data was used for training and 30% for testing. The accuracy of the model was evaluated as shown in Table 4. The quantitative evaluation metrics of the LSTM all proved that the method was effective in predicting time series deformation.

The LSTM was then used to predict the missing data from February to June 2019 (after the end of the TSX time series; see Figure 5) and combine these results with the following S1 data using the minimum gradient method to obtain a complete longest time-series deformation curve of the test PS points from 2011 to 2021 as shown in Figure 10.

We observed that the predictions of the algorithm showed high consistency with the reference PS-InSAR deformation curve and no outliers were found, showing the reliability of the algorithm. The fusion time point chosen by the method of minimum value of the gradient difference also makes the whole fusion curve very smooth. The comparison between the 2011–2021 fusion results and the CSK 2011–2020 reference time series is shown in Figure 11. The fused deformation curve basically matches the reference curve, which demonstrates that the algorithm achieves accurate fusion results.

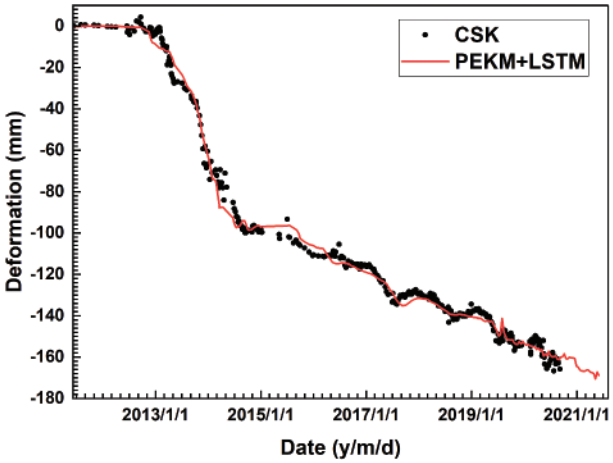

Figure 11. Comparison of the fused 2011–2021 time series obtained using the PEKM and LSTM proposed algorithm with the 2011–2020 reference deformation curve.

4.3. Time-lapse subsidence over Wuhan

The subsidence map derived at city scale from the fused subsidence time series is shown in Figure 12, illustrating the yearly cumulative subsidence from 2012 to 2021, where the changes in subsidence trends in the Wuhan area can be clearly seen. The study shows that the subsidence in Wuhan is influenced by both human and geological factors. The geological map of Wuhan area is shown in Figure 13. Subsidence in the Hankou area began to occur and gradually increase in 2013, reaching its maximum settlement and becoming stable in 2017–2018. This is mainly due to the soft soil consolidation in this area, accompanied by a certain amount of anthropogenic influence due to the construction of large buildings and subways which we previously reported in our study (Jiang et al. 2021). However, benefiting from the longer subsidence time series obtained in this paper, it can be seen that subsidence in the area has stabilized in 2018. Subsidence in the Wuchang and Hongshan Districts started later, around 2016–2017, and was still ongoing in 2021. This is because the area is geologically influenced by carbonate karstification and soft soils consolidation, and because these two districts are residential, therefore the extraction of groundwater during building construction and also

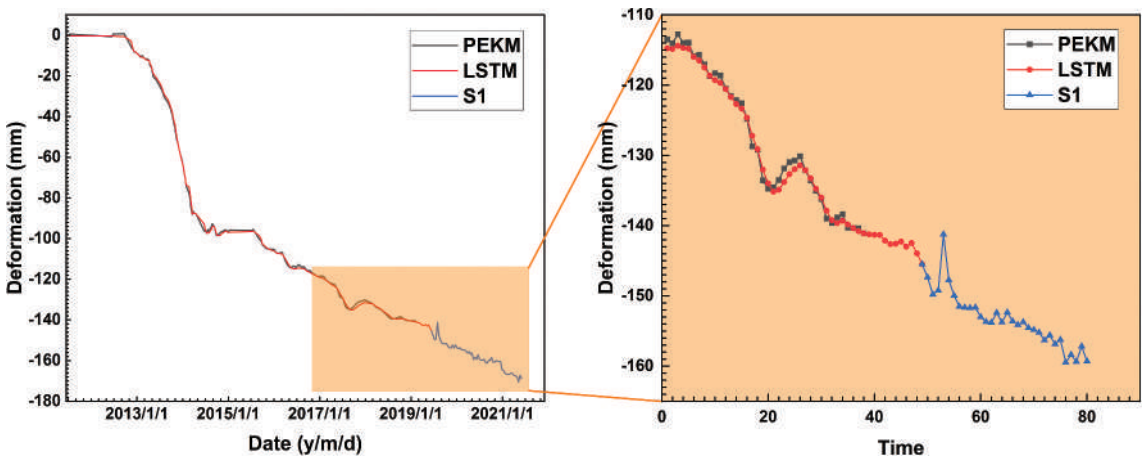

Figure 10. Temporal gap prediction and fusion result.

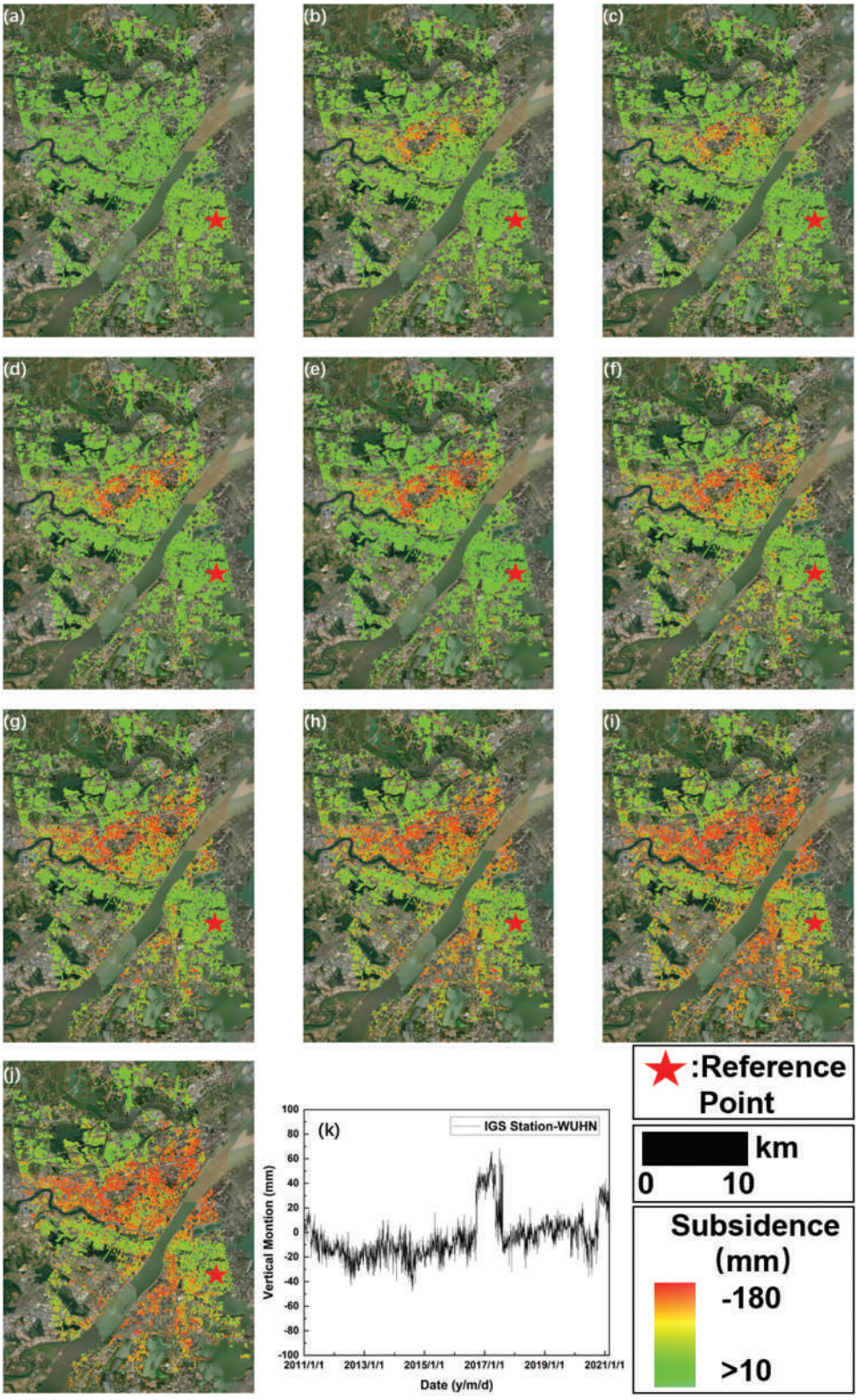

Figure 12. Time-lapse of subsidence in Wuhan based on the fused results, from 2012 (a) to 2021 (j). (k) Vertical motion of the reference point IGS stations (wuhn) from 2011 to 2019 (Han et al. 2020). The station underwent antenna replacement on September 21, 2016 due to antenna failure, and the replacement led to the abrupt changes, which was later restored to stability. Therefore, we chose this point as the reference point (data source: https://files.igs.org/pub/station/log_9char/wuhn00chn_20191209.log).

for living is a major anthropogenic factor contributing to the settlement process. This can be found in the studies by Jiang et al. (2021), Han et al. (2020) and Tapete et al. (2021) with a corresponding illustration.

Additionally, in the years in which the two algorithms fused the datasets (2015 across the overlapping period, and 2019 for the temporal gap), our algorithms did not reveal a cumulative error similar to that

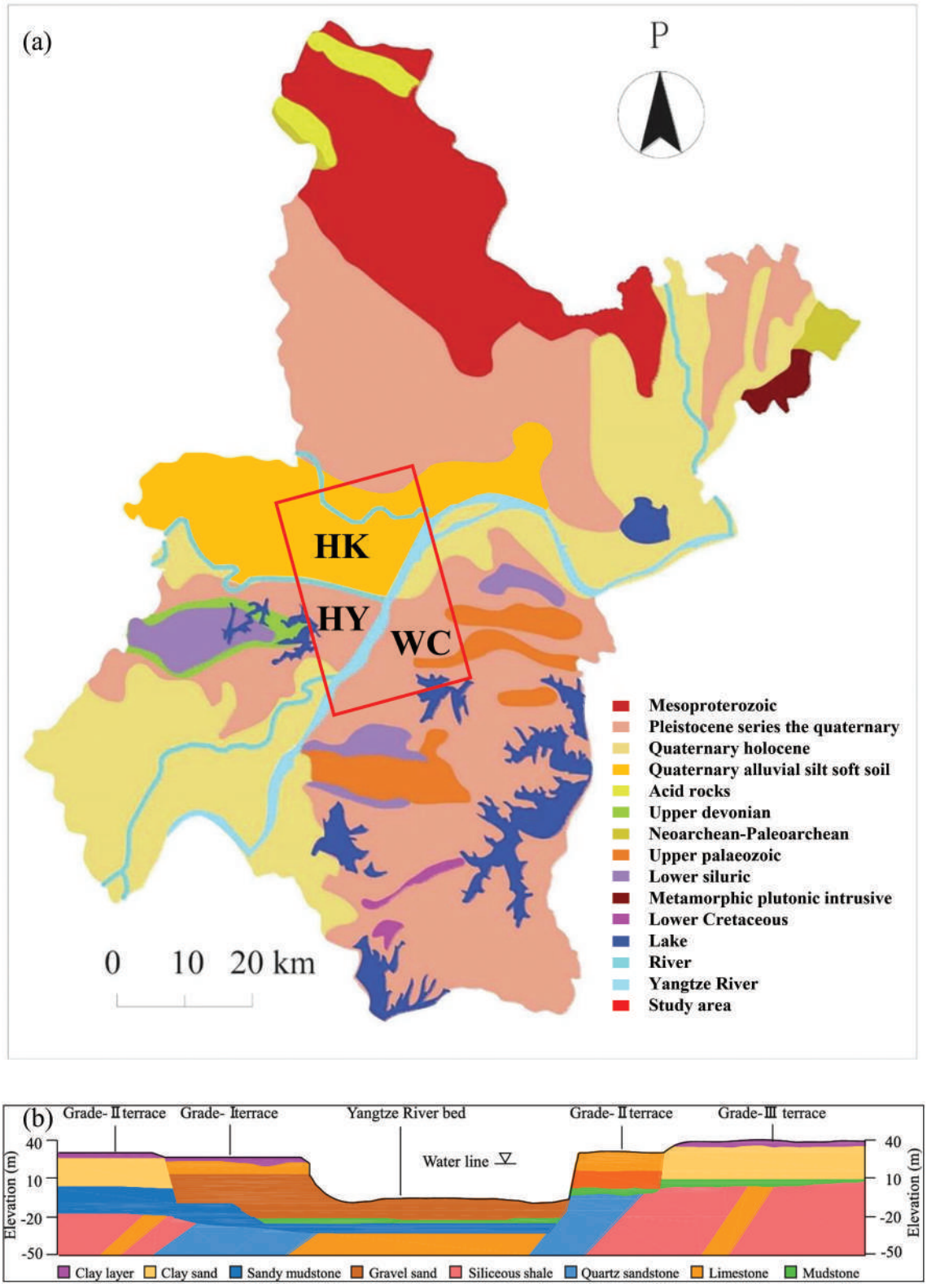

Figure 13. Simplified geological map of Wuhan, where units are grouped by age (modified from (Wu et al. 2020)). HK, HY and WC in the red rectangular, i.e. research area, are the abbreviations of Hankou, Hanyang and Wuchang, respectively. (b) Typical cross-section of Wuhan's geological structure, with details on lithologies and their thickness (reproduced from (Wang et al. 2020b)). Figure reproduced from (Jiang et al. 2021).

generated by the traditional algorithm in Figure 8. Based on the test undertaken over Wuhan, it is envisaged that the proposed method could be used to keep fusing data acquired continuously to update the subsidence data with further predictions, thus overcoming the potentially limited lifetime of a satellite mission, and further extending the series for a number of additional dates in the future. However, this will not enable the prediction of any nonlinearities, accelerations or decelerations in the deformation

trend that might occur due to other triggers and factors, such as accelerated subsidence due to new engineering works or augmented groundwater pumping, which cannot be predicted by the fusion method or anticipated in such a highly dynamic urban environment. Therefore, if a more refined study is needed, more influencing factors such as changes in groundwater, urban infrastructure construction, rainfall, and changes in land type need to be incorporated in the model. And the relevant analysis needs to be combined with engineering geological investigations.

5. Conclusions

A method is proposed for fusing InSAR deformation time series datasets from different SAR missions and/or time periods, which tackles the practical difficulties that typically arise when multi-sensor data are collected and analyzed to assess long-term land subsidence. The proposed method combines the PEKM with the LSTM neural network to fuse datasets where there are overlapping periods and temporal gaps in the multi-sensor time series. The algorithm was applied to fuse CSK, TSX, and S1 datasets collected over the city of Wuhan, which has been used as experiment area to model long-term deformation. A comparison of these results with a reference deformation time series and with subsidence trends reported in existing studies (Jiang et al. 2021; Hu et al. 2022; Han et al. 2020), shows the reliability of the proposed method. Experiments demonstrate that the method is an effective and complete algorithm for fusing multi-sensor InSAR deformation data to obtain long time series from historical data. It also serves as a means to update recent data to extend the series to embed future dates, essentially attempting to solve the problems associated with the limited length of some datasets. The method significantly improves the length of time series data for observed fast-evolving subsidence urban areas like Wuhan and provides a more effective basis for related subsidence mechanism studies.

Disclosure statement

No potential conflict of interest was reported by the author (s).

Funding

This work is funded by the National Natural Science Foundation of China [grant number 42250610212] and the China Scholarship Council [No. 202106270150].

Notes on contributors

Haonan Jiang is a PhD student at Wuhan University. He is a visiting PhD student at the Helmholtz Centre Potsdam, GFZ German Research Centre for Geosciences. His research interests incloud using radar remoting and SAR Interferometry to detect and analysis natural and anthropogenic hazards.

Timo Balz is a professor for radar remote sensing with the State Key Laboratory of Information Engineering in Surveying, Mapping and Remote Sensing, Wuhan University. He received his PhD degree in aerospace engineering and geodesy from Stuttgart University, Germany, in 2007. His research interests include radar remote sensing, SAR Interferometry and using SAR to support archaeological prospections.

Francesca Cigna is a senior researcher in Earth Observation at the Institute of Atmospheric Sciences and Climate (ISAC), National Research Council (CNR) of Italy. She received the PhD degree in Earth Sciences, and her research interests are SAR, advanced InSAR methods, data analytics, mapping and monitoring of natural/anthropogenic hazards in urban/rural environments.

Deodato Tapete is a researcher in Earth Observation and data analytics at the Italian Space Agency (ASI). He received the PhD degree in Earth Sciences, and his research interests are SAR and InSAR techniques applied to natural hazards, urban remote sensing, archaeological prospection and cultural heritage conservation.

Jianan Li is a PhD student at Liaoning technical university. Her research topic include SAR remote sensing and target detection.

Yakun Han is a lecturer at the College of Earth Sciences, Chengdu University of Technology. He received the PhD degree in Geodesy and Geomatics Engineering from Wuhan University in 2021. His research interests include land subsidence monitoring and characterization with InSAR, landslides monitoring with InSAR and modeling.

ORCID

Haonan Jiang http://orcid.org/0000-0002-8036-4300
Timo Balz http://orcid.org/0000-0002-1624-4697
Francesca Cigna http://orcid.org/0000-0001-8134-1576
Deodato Tapete http://orcid.org/0000-0002-7242-4473
Jianan Li http://orcid.org/0000-0001-8398-4962
Yakun Han http://orcid.org/0000-0002-7929-2581

Data availability statement

Data that support the results and analyses presented in this paper are freely available online or can be accessed through ad hoc data license agreements. In particular: Sentinel-1 data are available via Copernicus Open Access Hub (https://scihub.copernicus.eu/dhus); the SRTM DEM can be download from NASA's data catalogs (https://search.earthdata.nasa.gov/search); Other datasets are licensed (i.e. COSMO-SkyMed® Products © Italian Space Agency were delivered under a license for use by ASI led by D. Tapete; and TerraSAR-X data were made available by DLR via MTH3764 project) and thus cannot be shared.

References

Abidin, H. Z., H. Andreas, I. Gumilar, Y. Fukuda, Y. E. Pohan, and T. Deguchi. 2011. "Land Subsidence of

Jakarta (Indonesia) and its Relation with Urban Development." *Natural Hazards* 59 (3): 1753–1771. doi:10.1007/s11069-011-9866-9.

Bagheri-Gavkosh, M., S. M. Hosseini, B. Ataie-Ashtiani, Y. Sohani, H. Ebrahimian, F. Morovat, and S. Ashrafi. 2021. "Land Subsidence: A Global Challenge." *The Science of the Total Environment* 778: 146193. doi:10.1016/j.scitotenv.2021.146193.

Berardino, P., G. Fornaro, R. Lanari, and E. Sansosti. 2002. "A New Algorithm for Surface Deformation Monitoring Based on Small Baseline Differential SAR Interferograms." *IEEE Transactions on Geoscience and Remote Sensing* 40 (11): 2375–2383. doi:10.1109/TGRS.2002.803792.

Chen, B., H. Gong, Y. Chen, K. Lei, C. Zhou, Y. Si, X. Li, Y. Pan, and M. Gao. 2021. "Investigating Land Subsidence and Its Causes Along Beijing High-Speed Railway Using Multi-Platform InSar and a Maximum Entropy Model." *International Journal of Applied Earth Observation and Geoinformation* 96 (December 2020): 102284. doi:10.1016/j.jag.2020.102284.

Chen, B.L.L., H. Yu, X. Zhang, Z. Li, J. Kang, Y. Yu, J. Yang, and L. Qin. 2022. "Time-Varying Surface Deformation Retrieval and Prediction in Closed Mines Through Integration of SBAS InSar Measurements and LSTM Algorithm." *Remote Sensing* 14 (3): 788. doi:10.3390/rs14030788.

Chen, L., X. Zhao, Y. Tang, and H. Zhang. 2018. "Parameters Fitting and Evaluation of Exponent Knothe Model Combined with InSar Technique." *Rock and Soil Mechanics* 39 (2): 423–431.

Chen, Y., Y. He, L. Zhang, Y. Chen, H. Pu, B. Chen, and L. Gao. 2021. "Prediction of InSar Deformation Time-Series Using a Long Short-Term Memory Neural Network." *International Journal of Remote Sensing* 42 (18): 6921–6944. doi:10.1080/01431161.2021.1947540.

Cigna, F., R. E. Ramírez, and D. Tapete. 2021. "Accuracy of Sentinel-1 PSI and SBAS InSar Displacement Velocities Against GNSS and Geodetic Leveling Monitoring Data." *Remote Sensing* 13 (23): 1–28. doi:10.3390/rs13234800.

Cigna, F., and D. Tapete. 2021. "Satellite InSar Survey of Structurally-Controlled Land Subsidence Due to Groundwater Exploitation in the Aguascalientes Valley, Mexico." *Remote Sensing of Environment* 254 (July 2020): 112254. doi:10.1016/j.rse.2020.112254.

Costantini, M., J. Bai, F. Malvarosa, F. Minati, F. Vecchioli, R. Wang, Q. Hu, J. Xiao, and J. Li. 2016. "Ground Deformations and Building Stability Monitoring by COSMO-Skymed PSP SAR Interferometry: Results and Validation with Field Measurements and Surveys." *International Geoscience and Remote Sensing Symposium (IGARSS)* 6847–6850. doi:10.1109/IGARSS.2016.7730787.

Deng, L., G. Liu, R. Zhang, X. Wang, B. Yu, J. Tang, and H. Zhang. 2016. "A Multi-Platform MC-SBAS Method for Extracting Long-Term Ground Deformation." *Acta Geodaetica et Cartgraphica Sinica* 45 (2): 213–223.

Ding, Q., Z. Shao, X. Huang, O. Altan, Q. Zhuang, and B. Hu. 2021. "Monitoring, Analyzing and Predicting Urban Surface Subsidence: A Case Study of Wuhan City, China." *International Journal of Applied Earth Observation and Geoinformation* 102: 102422. doi:10.1016/j.jag.2021.102422.

Ferretti, A., C. Prati, and F. Rocca. 2000. "Nonlinear Subsidence Rate Estimation Using Permanent Scatterers in Differential SAR Interferometry." *IEEE Transactions on Geoscience and Remote Sensing* 38 (5 I): 2202–2212. doi:10.1109/36.868878.

Ferretti, A., C. Prati, and F. Rocca. 2001. "Permanent Scatterers in SAR Interferometry." *IEEE Transactions on Geoscience and Remote Sensing* 39 (1): 8–20. doi:10.1109/36.898661.

Gers, F. A., J. Schmidhuber, and F. Cummins. 1999. "Learning to Forget: Continual Prediction with LSTM." *IEE Conference Publication* 2 (470): 850–855. doi:10.1049/cp:19991218.

Haghshenas Haghighi, M., and M. Motagh. 2019. "Ground Surface Response to Continuous Compaction of Aquifer System in Tehran, Iran: Results from a Long-Term Multi-Sensor InSar Analysis." *Remote Sensing of Environment* 221 (March 2018): 534–550. doi:10.1016/j.rse.2018.11.003.

Han, Y., J. Zou, Z. Lu, F. Qu, Y. Kang, and J. Li. 2020. "Ground Deformation of Wuhan, China, Revealed by Multi-Temporal Insar Analysis." *Remote Sensing* 12 (22): 1–24. doi:10.3390/rs12223788.

Herrera-García, G., P. Ezquerro, R. Tomas, M. Béjar-Pizarro, J. López-Vinielles, M. Rossi, R. M. Mateos, et al. 2021. "Mapping the Global Threat of Land Subsidence." *Science* 371 (6524): 34–36. doi:10.1126/science.abb8549.

Hochreiter, S., and J. Schmidhuber. 1997. "Long Short-Term Memory." *Neural Computation* 9 (8): 1735–1780. doi:10.1162/neco.1997.9.8.1735.

Hu, J., M. Motagh, J. Guo, M. H. Haghighi, T. Li, F. Qin, and W. Wu. 2022. "Inferring Subsidence Characteristics in Wuhan (China) Through Multitemporal InSar and Hydrogeological Analysis." *Engineering Geology* 297: 106530. doi:10.1016/j.enggeo.2022.106530.

Hu, J., M. Motagh, J. Wang, F. Qin, J. Zhang, W. Wu, and Y. Han. 2021. "Karst Collapse Risk Zonation and Evaluation in Wuhan, China Based on Analytic Hierarchy Process, Logistic Regression, and Insar Angular Distortion Approaches." *Remote Sensing* 13 (24): 1–20. doi:10.3390/rs13245063.

Jiang, H., T. Balz, F. Cigna, and D. Tapete. 2021. "Land Subsidence in Wuhan Revealed Using a Non-Linear PSInSar Approach with Long Time Series of COSMO-Skymed SAR Data." *Remote Sensing* 13 (7): 1–17. doi:10.3390/rs13071256.

Lanari, R., O. Mora, M. Manunta, J. J. Mallorquí, P. Berardino, and E. Sansosti. 2004. "A Small-Baseline Approach for Investigating Deformations on Full-Resolution Differential SAR Interferograms." *IEEE Transactions on Geoscience and Remote Sensing* 42 (7): 1377–1386. doi:10.1109/TGRS.2004.828196.

Lei, C., Z. Xuesheng, T. Yixian, and Z. Hong. 2018. "Parameters Fitting and Evaluation of Exponent Knothe Model Combined with InSar Technique." *Rock and Soil Mechanics* 39 (Supp.2): 423–431.

Liu, Y., S. Cao, and Y. Liu. 2009. "The Improved Knothe Time Function for Subface Subsidence." *Science of Surveying and Mapping* 34 (5): 16–18.

Luo, X., and J. Shen. 2018. "Research Progress and Prospect of Karst Ground Collapse in China." *CARSO-LOGICA SINICA* 37 (1): 101–111.

Ma, D., M. Motagh, G. Liu, R. Zhang, X. Wang, B. Zhang, W. Xiang, and B. Yu. 2022. "Thaw Settlement Monitoring and Active Layer Thickness Retrieval Using Time Series COSMO-Skymed Imagery in Iqaluit Airport." *Remote Sensing* 14 (9): 2156. doi:10.3390/rs14092156.

Orhan, O. 2021. "Monitoring of Land Subsidence Due to Excessive Groundwater Extraction Using Small Baseline

Subset Technique in Konya, Turkey." *Environmental Monitoring and Assessment* 193 (4): 1–17. doi:10.1007/s10661-021-08962-x.

Orhan, O., T. Oliver-Cabrera, S. Wdowinski, S. Yalvac, and M. Yakar. 2021. "Land Subsidence and Its Relations with Sinkhole Activity in Karapınar Region, Turkey: A Multi-Sensor Insar Time Series Study." *Sensors (Switzerland)* 21 (3): 1–17. doi:10.3390/s21030774.

Pepe, A., G. Solaro, F. Calò, and C. Dema. 2016. "A Minimum Acceleration Approach for the Retrieval of Multiplatform InSar Deformation Time Series." *IEEE Journal of Selected Topics in Applied Earth Observations and Remote Sensing* 9 (8): 3883–3898. doi:10.1109/JSTARS.2016.2577878.

Perissin, D., Z. Wang, and H. Lin. 2012. "Shanghai Subway Tunnels and Highways Monitoring Through Cosmo-SkyMed Persistent Scatterers." *ISPRS Journal of Photogrammetry and Remote Sensing* 73: 58–67. doi:10.1016/j.isprsjprs.2012.07.002.

Pratesi, F., D. Tapete, C. Del Ventisette, and S. Moretti. 2016. "Mapping Interactions Between Geology, Subsurface Resource Exploitation and Urban Development in Transforming Cities Using InSar Persistent Scatterers: Two Decades of Change in Florence, Italy." *Applied Geography* 77: 20–37. doi:10.1016/j.apgeog.2016.09.017.

Qu, X., J. Yang, and M. Chang. 2019. "A Deep Learning Model for Concrete Dam Deformation Prediction Based on RS-LSTM." *Journal of Sensors* 2019: 1–14. doi:10.1155/2019/4581672.

Roccheggiani, M., D. Piacentini, E. Tirincanti, D. Perissin, and M. Menichetti. 2019. "Detection and Monitoring of Tunneling Induced Ground Movements Using Sentinel-1 SAR Interferometry." *Remote Sensing* 11 (6): 639. doi:10.3390/rs11060639.

Samsonov, S., and N. D'Oreye. 2012. "Multidimensional Time-Series Analysis of Ground Deformation from Multiple InSar Data Sets Applied to Virunga Volcanic Province." *Geophysical Journal International* 191 (3): 1095–1108. doi:10.1111/j.1365-246X.2012.05669.x.

Sherstinsky, A. 2020. "Fundamentals of Recurrent Neural Network (RNN) and Long Short-Term Memory (LSTM) Network." *Physica D Nonlinear Phenomena* 404: 132306. doi:10.1016/j.physd.2019.132306.

Stramondo, S., F. Bozzano, F. Marra, U. Wegmuller, F. R. Cinti, M. Moro, and M. Saroli. 2008. "Subsidence Induced by Urbanisation in the City of Rome Detected by Advanced InSar Technique and Geotechnical Investigations." *Remote Sensing of Environment* 112 (6): 3160–3172. doi:10.1016/j.rse.2008.03.008.

Sun, Q., J. Hu, L. Zhang, and X. Ding. 2016. "Towards Slow-Moving Landslide Monitoring by Integrating Multi-Sensor InSar Time Series Datasets: The Zhouqu Case Study, China." *Remote Sensing* 8 (11): 1–16. doi:10.3390/rs8110908.

Tan, R., Y. Liu, Y. Liu, Q. He, L. Ming, and S. Tang. 2014. "Urban Growth and Its Determinants Across the Wuhan Urban Agglomeration, Central China." *Habitat Internatio-nal* 44: 268–281. doi:10.1016/j.habitatint.2014.07.005.

Tapete, D., F. Cigna, T. Balz, H. Tanveer, J. Wang, and H. Jiang. 2021. "Multi-Temporal InSar and Target Detection with COSMO-Skymed SAR Big Data to Monitor Urban Dynamics in Wuhan (China)." *International Geoscience and Remote Sensing Symposium (IGARSS)* 2021: 3793–3796.

Wang, J., T. Balz, and M. Liao. 2016. "Geo-Spatial Information Science Absolute Geolocation Accuracy of High-Resolution Spotlight TerraSAR-X Imagery – Validation in Wuhan." *Geo-Spatial Information Science* 19 (4): 267–272. doi:10.1080/10095020.2016.1258183.

Wang, X., J. Lai, S. He, R. S. Garnes, and Y. Zhang. 2020a. "Karst Geology and Mitigation Measures for Hazards During Metro System Construction in Wuhan, China." *Natural Hazards* 103 (3): 2905–2927. doi:10.1007/s11069-020-04108-3.

Wang, X., J. Lai, S. He, R. S. Garnes, and Y. Zhang. 2020b. "Karst Geology and Mitigation Measures for Hazards During Metro System Construction in Wuhan, China." *Natural Hazards* 103 (3): 2905–2927. doi:10.1007/s11069-020-04108-3.

Wu, H. L., W. C. Cheng, S. L. Shen, M. Y. Lin, and A. Arulrajah. 2020. "Variation of Hydro-Environment During Past Four Decades with Underground Sponge City Planning to Control Flash Floods in Wuhan, China: An Overview." *Underground Space (China)* 5 (2): 184–198. doi:10.1016/j.undsp.2019.01.003.

Xing, X., Y. Zhu, W. Xu, W. Peng, and Z. Yuan. 2022. "Measuring Subsidence Over Soft Clay Highways Using a Novel Time-Series InSar Deformation Model with an Emphasis on Rheological Properties and Environmental Factors (NREM)." *IEEE Transactions on Geoscience and Remote Sensing* 60: 1–19. doi:10.1109/TGRS.2022.3154430.

Xinru, Z., and L. Yuchan. 2012. "Knothe Time Functions and Their Application in Dynamic Subsidence on the Ground." *Surveying and Mapping of Geology and Mineral Resources* 28 (3): 14–20. doi:10.16864/j.cnki.dkch.2012.03.006.

Yao, L., and W. A. Sethares. 1994. "Nonlinear Parameter Estimation via the Genetic Algorithm." *IEEE Transaction on Signal Processing* 42 (4): 927–935. doi:10.1109/78.285655.

Yastika, P. E., N. Shimizu, and H. Z. Abidin. 2019. "Monitoring of Long-Term Land Subsidence from 2003 to 2017 in Coastal Area of Semarang, Indonesia by SBAS DInSar Analyses Using Envisat- ASAR, ALOS-PALSAR, and Sentinel-1A SAR Data." *Advances in Space Research* 63 (5): 1719–1736. doi:10.1016/j.asr.2018.11.008.

Zebker, H. A., and R. M. Goldstein. 1986. "Topographic Mapping from Interferometric Synthetic Aperture Radar Observations." *Journal of Geophysical Research* 91 (B5): 4993–4999. doi:10.1029/JB091iB05p04993.

Zhou, C., Y. Cao, X. Hu, K. Yin, Y. Wang, and F. Catani. 2022. "Enhanced Dynamic Landslide Hazard Mapping Using MT-Insar Method in the Three Gorges Reservoir Area." *Landslides* 19 (7): 1585–1597. doi:10.1007/s10346-021-01796-1.

Zhou, C., Y. Cao, K. Yin, E. Intrieri, F. Catani, and L. Wu. 2022. "Characteristic Comparison of Seepage- Driven and Buoyancy-Driven Landslides in Three Gorges Reservoir Area, China." *Engineering Geology* 301 (February): 106590. doi:10.1016/j.enggeo.2022.106590.

Zhou, L., J. Guo, J. Hu, J. Li, Y. Xu, Y. Pan, and M. Shi. 2017. "Wuhan Surface Subsidence Analysis in 2015–2016 Based on Sentinel-1A Data by SBAS-Insar." *Remote Sensing* 9 (10): 982. doi:10.3390/rs9100982.

Zhu, L., H. Gong, X. Li, R. Wang, B. Chen, Z. Dai, and P. Teatini. 2015. "Land Subsidence Due to Groundwater Withdrawal in the Northern Beijing Plain, China." *Engineering Geology* 193: 243–255. doi:10.1016/j.enggeo.2015.04.020.